Materials Advances

ROYAL SOCIETY OF CHEMISTRY

PAPER

View Article Online
View Journal | View Issue

Cite this: *Mater. Adv.*, 2024, 5, 7700

Highly tensile and sensitive strain sensors with micro–nano topology optimization†

Weixia Lan, [a] Qiqi Ding,[a] Tao Zhou,[a] Zilong Guo,[a] Wenbin Sun,[a] Zhenghui Wu, *[b] Yingjie Liao,*[a] Bin Wei [a] and Yuanyuan Liu *[a]

Received 15th July 2024,
Accepted 21st August 2024

DOI: 10.1039/d4ma00715h

rsc.li/materials-advances

With the extensive application of flexible sensors in various wearable electronics being continuously explored, researchers are paying more and more attention to improving their sensitivity while ensuring high stretchability. In this study, a novel fiber strain sensor was proposed with micro–nano topology optimization, which was achieved through a simple, cost-effective and scalable method. A TPU/PEO substrate was prepared by electrospinning technology, then the fibrous membrane was immersed in deionized water to wash away the PEO and obtain the micro–nano topological structure. Carbon nanotubes (CNTs) and graphene were further adsorbed on the etched TPU fibrous membrane through ultrasonic treatment to obtain TPU:PEO/CNTs and TPU:PEO/graphene sensors, respectively. Both experimental and simulation results showed that the optimization of the PEO ratio is crucial for the balance between wide deformation and high sensitivity. A wide detection range (0–650%) and high sensitivity (GFmax = 976.89) were obtained for the TPU:PEO/graphene sensor, demonstrating its suitability for high-performance strain sensors. It can not only capture minor human movements, but also be effectively applied in fitness scenarios, which may contribute to personalized scientific training and reduce sports injuries.

1. Introduction

Flexible strain sensors are crucial in wearable technology for sports and health monitoring, electronic skin, and soft robotics.[1–5] They are expected to have a wide deformation range, high sensitivity, and long durability.[6–10] High sensitivity and a wide detection range are required to capture both subtle human movement signals[11] and large joint motion signals.[12] Researchers have explored various elastic substrates and conductive material and structural designs to achieve tunable and high-performance strain-responsive sensors.[13,14] Elastic materials including thermoplastic polyurethane (TPU), polydimethylsiloxane (PDMS), rubber (RB), and hydrogels are usually used as flexible substrates for wide detection limits.[15–18] Conductive materials such as carbon black, graphene, carbon nanotubes (CNTs), and silver nanowires are commonly being integrated to enhance sensitivity.[19–22] Structural design includes fiber structures from the micro- to macro-scale, such as fiber orientation, fiber geometry and the geometry formed between fibers.[23]

TPU is very widely utilized in the fabrication of sensors with a broad sensing range due to its exceptional elastic properties.[24,25] Liu *et al.*[26] reported a TPU-based flexible piezoresistive sensor coated with MXenes/CNTs, achieving stable sensing over a wide operating range of up to 700% in the tensile mode, with a gauge factor (GF) value of 17.8. Jia *et al.*[27] introduced polyacrylonitrile (PAN) into TPU and prepared highly conductive and stretchable MXene/TPU/PAN membranes, achieving a detection range of up to 200% with a GF of 9.96. However, the results indicate that simply integrating conductive materials on flexible substrates is insufficient to meet the high sensitivity requirements for actual applications. Various novel microstructures have been recently developed to further enhance the sensor sensitivity, such as porous structures, wrinkled structures, microcrack structures,[28] and interlocking structures.[29–32] Especially, constructing a porous structure can significantly enhance the adhesion of conductive materials,[33] promoting the formation of a continuous conductive path and thus increasing its sensitivity.[34–39]

For instance, Yuan *et al.*[40] proposed an effective morphology control method combining melt blending and chemical etching and achieved a high sensitivity sensor with a GF value of 1189.1, where CNTs were uniformly dispersed in TPU foam forming a uniform three-dimensional conductive network. Niu *et al.*[41] prepared a fiber strain sensor with a wide detection limit (200%) and high sensitivity (GF = 2.52 × 10^4) by wet spinning porous methods. Concurrently, the suitability for large-scale fabrication

[a] *School of Mechatronic Engineering and Automation, Shanghai University, Shanghai 200444, China. E-mail: yjliao@shu.edu.cn, yuanyuan_liu@shu.edu.cn*
[b] *Key Laboratory for Special Functional Materials of Ministry of Education, School of Nanoscience and Materials Engineering, Henan University, Kaifeng 475004, China. E-mail: wuzhenghuihk@henu.edu.cn*

† Electronic supplementary information (ESI) available: Highly tensile and sensitive strain sensors with micro–nano topology optimization. See DOI: https://doi.org/10.1039/d4ma00715h

is also one of the critical factors to be considered in the manufacturing of sensors.[42] However, it is still challenging to use simple and convenient methods to introduce porous structures and balance the sensitivity and detection range.

In this work, a highly tensile and sensitive strain sensor was designed with micro–nano topology optimization. A TPU/PEO flexible substrate was prepared by electrospinning technology and then etched with deionized water to create micro–nano topological structures, including the rough structure of a single fiber and the porous structure formed by multiple fiber overlap. Results showed that the optimization of the PEO ratio was crucial for the balance between wide deformation and high sensitivity. By optimizing the ratio of PEO, high sensitivity (GFmax = 98.52) and a wide detection range (0–450%) were achieved for the TPU:PEO/CNTs sensor. The TPU/PEO membrane was immersed in deionized water to wash away the PEO and obtain the micro–nano topological structure. With the etching of optimal PEO, the fiber surface showed increased roughness, resulting in overlap and adhesion between fibers and forming the best pore structure for the further absorption of conductive materials. Furthermore, carbon nanotubes (CNTs) and graphene were adsorbed on the etched TPU fibrous membrane through ultrasonic treatment to obtain the TPU:PEO/CNTs and TPU:PEO/graphene sensors, respectively. A wider detection range (0–650%) and higher sensitivity (GFmax = 976.89) are also obtained for the TPU:PEO/graphene sensor, demonstrating its suitability as a versatile strain sensor. This sensor can be used for monitoring minor movements and detecting human activities such as breathing, swallowing, and finger bending with different angles. Furthermore, it is successfully applied to posture recognition and correction in fitness exercises, demonstrating its feasibility in wearable electronics.

2. Materials and methods

2.1. Materials

Polyester-based TPU (Elastollan 1185A) was bought from Xing yuan Plastic Raw Material Store. The multi-walled CNTs (TNIM2) were purchased from Chengdu Organic Chemicals, Chinese Academy of Sciences.

Tetrahydrofuran (THF, 99.5%), *N*,*N*-dimethylformamide (DMF), anhydrous ethanol (99.5%), and polyethylene oxide (PEO) were provided by Aladdin Biochemical Technology Co., Ltd.

2.2. Preparation of TPU/PEO nanofiber membranes

First, as shown in Fig. 1a, TPU granules and PEO powder (with mass ratios of 2 g : 0.2 g, 2 g : 0.4 g, and 2 g : 0.6 g) were dissolved in 10 mL of a DMF/THF mixture (DMF/THF volume ratio of 3 : 2). The mixed solution was heated to 60 °C and stirred magnetically for complete dissolution, which was then filled into 20 mL syringes for electrospinning. A 9 kV voltage was applied between the needle tip and the collecting plate at a working distance of 15 cm. The TPU/PEO fibers were collected at a rate of 1.0 mL h^{-1}. Finally, the nanofiber membranes were removed, dried, stored, and cut into appropriate sizes for further use. The nanofiber membranes obtained with different ratios were immersed in deionized water at room temperature for 24 hours to wash away the PEO and then dried at 35 °C for 4 hours to obtain etched TPU membranes with porous micro–nano topology, which are named pure-TPU, TPU/PEO2, TPU/PEO4, and TPU/PEO6.

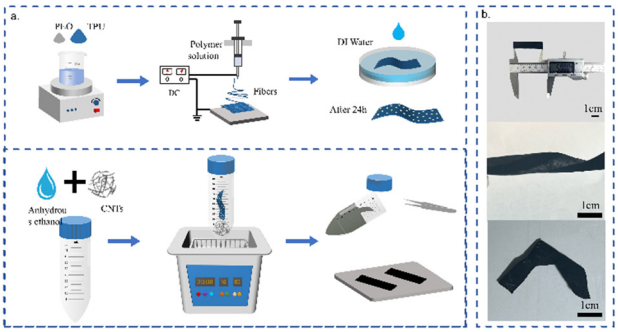

Fig. 1 (a) Preparation process of TPU:PEO/CNTs sensors; (b) physical drawing of TPU:PEO/CNTs.

2.3. Preparation of TPU:PEO/CNTs strain sensors

Subsequently, CNTs (0.3 g, 0.9 g, and 1.5 g) were added to 30 mL of anhydrous ethanol and ultrasonically treated for 60 minutes to prepare carbon nanotube dispersions with concentrations of 1%, 3%, and 5%. To form a complete conductive network, the etched TPU fiber membranes were then immersed in a well-dispersed CNT suspension through repeated ultrasonic treatment. Finally, the aligned TPU:PEO/CNTs sensors were washed with deionized water and dried at 60 °C for 4 hours. Then, a conductive fabric tape was attached to both ends to fabricate TPU:PEO/CNTs strain sensors. In addition, the same etching method was used to fabricate TPU/graphene strain sensors with a 3% concentration of graphene dispersion. For the convenience of testing, the TPU:PEO/CNTs sensor was cut into strips of 50 × 10 mm^2. To ensure the accuracy of the results, more than 10 samples were tested in each experiment. The sensor showed good tensile elasticity and can be bent and knotted, as shown in Fig. 1b.

2.4. Characterization

The microstructure was observed by using a SEM (Hitachi SU8230), the functional group changes before and after etching were observed using a Fourier transform infrared (FT-IR) spectrometer (ALPHA, BRUKER, Karlsruhe, Germany), and the resistance was measured using a flexible electronic performance test platform (Prtronic flexible electronic test platform, Shanghai Prtronic Electronic Technology Co. Ltd). The stress–strain characteristics were captured using an air bath tensile tester (KNWN-K500D, Jinan KNTEST Testing Machine Manufacturing Co. Ltd).

2.5. Ethical statement

All experiments were performed in compliance with the relevant guidelines. The ethics committee of Shanghai University

has approved the study with the approval number ECSHU2023-041. Informed consent was obtained from human participants.

3. Results and discussion

3.1. Morphology and tensile properties of TPU/PEO nanofiber membranes with topology

As can be seen from Fig. 2a, the overall structure of pure-TPU nanofibers is smooth, and the fiber diameter is uniformly 0.65 μm as shown in Fig. S1a (ESI†), and the locally enlarged view is shown in Fig. 2a$_1$.

As shown in Fig. 2b, the etched TPU/PEO2 nanofiber membrane displayed a pore structure formed by fiber overlap. The enlarged view shown in Fig. 2b$_1$ revealed that the etched TPU/PEO2 nanofiber membrane began to develop a rough surface. With the addition and etching of PEO, the fiber surface showed increased roughness, resulting in overlap and adhesion between fibers and forming a porous structure. Observations from Fig. 2c and c$_1$ indicated that, as the PEO concentration increased to 4%, the roughness and porosity of the fibers also increased. The porosity of the TPU/PEO2 nanofiber membrane was about 43.79% at a 2% PEO concentration, and it reached 53.77% when the PEO concentration increased to 4%. The TPU/PEO6 nanofiber membrane showed adhesion and could not be formed into fibers during the spinning process. Due to the high PEO concentration, the TPU/PEO composite solution was too viscous, resulting in poor spinning results. As shown in Fig. S1b (ESI†), the solution accumulated on a large area of the nanofiber membrane, and the TPU/PEO6 fibers were excessively adhered. Fig. S2 (ESI†) illustrates the changes in the roughness of the fiber membranes after the addition of PEO and subsequent etching, as observed through a SEM image with higher magnification. It also compares the morphology with the SEM image of the nanofiber membranes before and after etching.

When PEO is added, the TPU/PEO nanofibers present a rough structure after etching, and the rough fibers are more likely to overlap to form micro–nano pores. After confirming that the addition of PEO induced microstructural changes, the masses of TPU/PEO2, TPU/PEO4, and TPU/PEO6 composite nanofiber membranes were measured before and after etching. The mass differences were then compared with the initial mass of PEO as determined in Section 2.1. As illustrated in Fig. 2d, the etching effect initially increased as the PEO concentration increased from 2% to 6%. The TPU/PEO4 membrane exhibited the optimal etching effect, with an etching rate of 64.2%. At a 4% PEO concentration, the area where PEO could mix with TPU was larger compared to a 2% concentration, resulting in a more effective etching process. However, at a 6% PEO concentration, the excess PEO became entangled within the individual fibers during the spinning process, leading to an incomplete etching effect and a reduced etching rate.

Furthermore, the mechanical properties of the TPU/PEO composite nanofiber membranes were investigated, as shown in Fig. 2e. TPU/PEO2, TPU/PEO4, and TPU/PEO6 nanofiber membranes were cut to the same size (50 × 10 mm^2) and stretched to fracture at a speed of 1 mm s^{-1} using a universal tensile testing machine. The results indicated that as the PEO ratio increased, the maximum stretching distance of the composite nanofiber membrane gradually decreased. This reduction was attributed to the relatively poor elastic properties of PEO. Consequently, the elastic properties of the composite nanofiber membrane deteriorated with higher PEO ratios. As depicted in Fig. 2e, the nanofiber membrane containing 6% PEO exhibited a maximum elongation of only 180%, significantly lower than the strain ranges observed in the other two composite fiber membrane groups. The decrease in the strain range could be attributed to the combined effects of the material composition and the fiber spinning process.

Therefore, based on a comprehensive balance between the spinning effect, morphology, etching ratio and tensile properties, the etching effect of the composite nanofiber membrane with a PEO ratio of 4% was chosen, and the etched TPU/PEO4 film was subsequently selected for sensor preparation.

At the same time, to reconfirm the etching of PEO in TPU/PEO4, Fourier transform infrared (FTIR) spectroscopy analysis was performed on the original unwashed composite fiber membrane with a PEO ratio of 4% (named TPU/PEO4-o) and the etched composite fiber membrane (TPU/PEO4). As shown in Fig. 2f, a bimodal feature was observed at 1730 cm^{-1} in the spectra of both systems. This phenomenon indicates the presence of an ester group (C═O) in both polyester and polyether polyurethane elastomeric segments, thus confirming the presence of an ester group in TPU.[43] Moreover, both membranes showed characteristic peaks related to C–O functional groups at 1110 cm^{-1}, but the peak intensity of TPU/PEO-o nanofiber membranes was higher than that of TPU/PEO4 nanofiber membranes, which may be due to the superposition effect of the polyurethane-based vibration and carbon–oxygen single bond

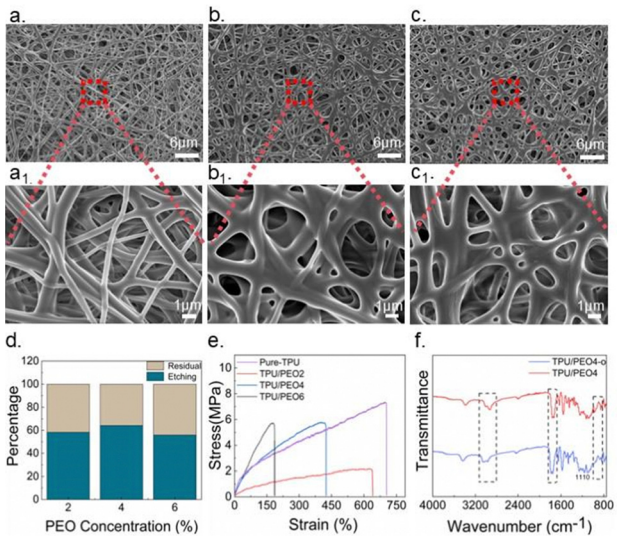

Fig. 2 SEM images of the (a) and (a$_1$) etched pure-TPU nanofiber membrane, (b) and (b$_1$) etched TPU/PEO2 nanofiber membrane, and (c) and (c$_1$) etched TPU/PEO4 nanofiber membrane; (d) variation of the etching rate of TPU/PEO2, TPU/PEO4, and TPU/PEO6 nanofiber membranes; (e) stress–strain graph of nanofibrous membranes with different PEO concentrations; and (f) FTIR spectroscopy images of unetched TPU/PEO4-o and TPU/PEO4 nanofibrous membranes.

expansion vibration in PEO. In particular, the doublet at 1070–1170 cm^{-1} in the FTIR spectrum of TPU/PEO4-o nanofiber membranes was due to the stretching vibration of the epoxy group in PEO. In the TPU/PEO4 system, the intensity of this doublet is significantly reduced, indicating that the PEO has been successfully removed, thus affecting the strength of its vibration mode.

3.2. Micro–nano topology and impregnated CNTs

After determining that the optimal concentration of PEO is 4%, the optimal concentration of impregnated CNTs was further discussed using the TPU/PEO4 nanofiber membrane. According to the different concentrations of CNTs, the prepared sensors are named TPU:PEO/CNTs1, TPU:PEO/CNTs3, and TPU:PEO/CNTs5. SEM images at three different concentrations were taken to observe the attachment morphology of CNTs on the fibers. In general, CNTs were either attached to the fiber surface or aggregated in the micropores, forming conductive paths and reflecting good interfacial compatibility between TPU and CNTs. With a 1.0% dispersion concentration of CNTs in the impregnation solution, only a small amount of CNTs were attached to the fiber surfaces and pores, leaving most areas undecorated. As the concentration of CNTs increased, the number of CNTs attached to the fibers and pores in the sensors also increased, and the fibers became more fully coated. At a 3.0% concentration, CNTs formed a dense layer on the TPU fiber surface and the fiber pores were strongly filled (Fig. 3b). However, at a 5.0% CNT concentration, large clusters of CNTs accumulated at the fiber joints, as shown in Fig. 3.

The response value of the strain sensor is expressed as R/R_0, where R is the transient resistance and R_0 is the initial resistance. Fig. 3d shows the resistance change rates of TPU:PEO/CNTs1, TPU:PEO/CNTs3, and TPU:PEO/CNTs5 sensors under the same stretching conditions. The TPU:PEO/CNTs3 sensor exhibited the highest resistance change rate. The reason is that when compared to the 1% concentration, the composite nanofiber membrane adsorbed more CNTs and formed more conductive channels as the concentration increased to 3%. At a 5% concentration, the large carbon nanotube clusters negatively affected sensing performance. The accumulation of conductive fillers also degraded the mechanical properties and the interaction between nanotubes and polymers. As a result, the sensor's performance at 5% was worse than at 3%. To verify the enhancement in sensing performance due to the etched micro–nano topological structure, a pure-TPU:PEO/CNTs3 sensor was prepared for comparison. Fig. 3d shows that the resistance change rate of pure-TPU:PEO/CNTs3 was much lower than that of TPU:PEO/CNTs3. Results confirmed that the introduction of a micro–nano topological structure helps improve sensor performance. The nanofiber film with micro–nano topology absorbed more CNTs under identical immersion conditions, enhancing sensor performance.

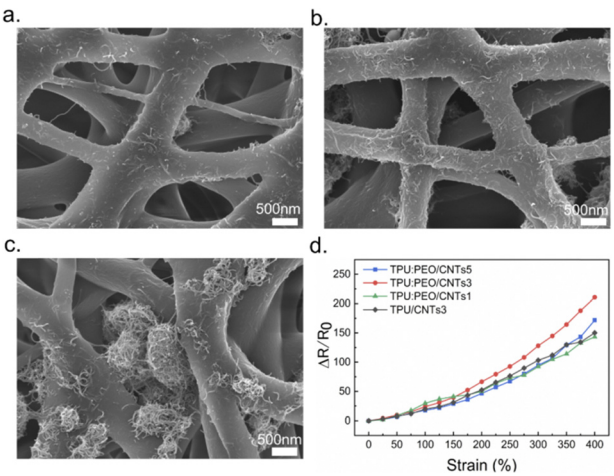

Fig. 3 SEM images of (a) TPU:PEO/CNTs1, (b) TPU:PEO/CNTs3 and (c) TPU:PEO/CNTs5 membranes; (d) sensing performance diagram of TPU/CNTs, TPU:PEO/CNTs1, TPU:PEO/CNTs3 and TPU/CNTs5.

Therefore, the micro–nano topology effectively improved sensor sensitivity. With an increased concentration of CNT dispersion, the CNT content on the impregnated substrate film also increased, forming more conductive paths and improving sensor sensitivity. However, an excessively high CNT content had a negative impact on sensing performance. Based on these results, a sensor impregnated with 3% CNTs was selected for further testing, referred to as the TPU:PEO/CNTs sensor. The final sensor showed an initial resistance of 4 kΩ.

To determine the modification effect of CNTs, thermogravimetric analysis (TGA) was performed. Fig. S3 (ESI†) shows the curves of TPU fibers before and after CNT modification. The decomposition process of TPU/CNTs is similar to that of TPU/PEO4, but the thermal decomposition temperature of TPU/CNTs is slightly lower than that of TPU/PEO4, indicating that CNTs can accelerate the decomposition of TPU. This could be ascribed to the high thermal conductivity of CNTs of up to 3000 W m^{-1} K^{-1}, which facilitates heat transfer to the inner layers of the composite material.[44] The mass difference before and after modification confirms that CNTs were successfully modified in the TPU fibers.

3.3. Principal explanation of the TPU/CNTs sensor with micro–nano topology

Fig. 4a illustrates the enhanced effect of micro–nano topology introduced by etching on the adsorption of conductive materials. After ultrasonic treatment with deionized water, the PEO in the composite TPU/PEO fiber was removed, resulting in a fine rough microstructure on the fiber surface. This process enriched the surface morphology of the material and significantly increased the surface contact area between individual fibers and CNTs. The increased contact area provided a stronger bonding foundation between CNTs and the TPU film during impregnation, thus enhancing adhesion. Simultaneously, the pore structure formed by the overlapping fibers provided more attachment points for CNTs. It contributed to more efficient adsorption of CNTs on the TPU surface, forming a denser and continuous conductive network. This improvement not only enhanced the conductivity of the material but also laid a solid foundation for subsequent sensor applications.

The TPU:PEO/CNTs sensor exhibited a significant strain-dependent performance variation during the tensile process, as depicted in Fig. 4b. Initially, within the low strain range, the

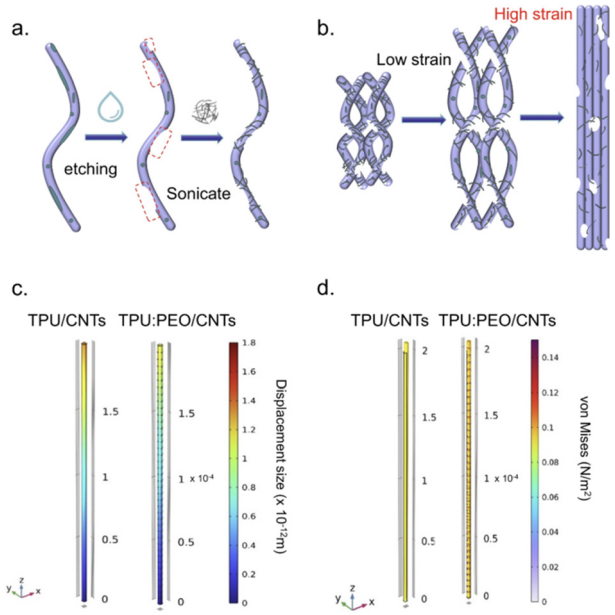

Fig. 4 (a) Schematic diagram of etching and impregnation; (b) schematic diagram of the tensile morphology change of the TPU:PEO/CNTs sensor with micro–nano topology after etching; (c) simulated displacement change diagram of the non-etched structure and sensor with an etched structure under the same stress; (d) stress distribution diagram of sensors with a non-etched structure and an etched structure under the same displacement.

composite filament transitioned mainly from a bent state to a straightened state. This operation caused some conductive channels to break due to the stretching. Meanwhile, as the stretch was minimal, most filaments were not fully straightened, thus keeping most of the conductive channels intact. Consequently, the principal modification was observed within the conductive network of CNTs on the fiber surface, yielding a relatively low sensor sensitivity. As stretching progressed to a high strain range, the situation substantially changed. The further elongation of the filament resulted in significant transformations of both the pore structure and the conductive network of CNTs on the filaments. This dramatic structural alteration led to a sudden augmentation in the sensitivity of the sensor. By virtue of its strain-dependent nature, the TPU:PEO/CNTs sensor could deliver varying sensitivity responses when subjected to different stretching degrees, hence showing broad adaptability for various application scenarios. Fig. S4 (ESI†) shows the SEM images corresponding to those in Fig. 4b. The process depicted in Fig. S4a and b (ESI†) corresponded to the sensor fiber morphology change with different deformation. When the deformation became significant, the fibers were stretched sharply and exhibited a highly aligned state as shown in Fig. S4c (ESI†).

To better demonstrate the performance advantages of the TPU:PEO/CNTs sensor, we utilized COMSOL software to simulate both the TPU:PEO/CNTs sensor with a microstructure and the TPU/CNTs sensor without a microstructure. Within the mechanical stress physics framework, an identical stress was applied to both sensor models. The simulation results of displacement changes under the same stress are depicted in Fig. 4c. It is evident that the displacement change of the TPU:PEO/CNTs sensor is smaller compared to the TPU/CNTs sensor. This difference is primarily attributed to the enhanced sensing performance provided by the microstructures. As a result, the TPU:PEO/CNTs sensor can detect a greater degree of force change with smaller displacement changes, thus resulting in a larger detection range. Furthermore, to investigate the specific stress variations experienced by the fibers during deformation, we examined the von Mises stress distribution in both the TPU:PEO/CNTs sensor and the TPU/CNTs sensor when subjected to the same physical conditions and displacement, as shown in Fig. 4d. When subjected to an equivalent strain displacement range, the TPU:PEO/CNTs sensor with the microstructure exhibited a greater stress response than the TPU/CNTs sensor. This confirms that the sensors with micro–nano topology can monitor larger substantial stress variations within the same deformation range.

3.4. Performance characterization of the sensor

Researchers typically introduce the concept of gauge factor (GF) to represent the sensitivity of strain sensors with the following formula:

$$\mathrm{GF} = \frac{\Delta R/R_0}{\Delta \varepsilon} \quad (1)$$

where R_0 is the initial resistance, ΔR indicates the resistance change, and $\Delta\varepsilon$ denotes the sensor strain. Fig. 5a shows that the ultrasonic-impregnated TPU:PEO/CNTs sensor maintained stable GF values across a broad range, supported by the micro–nano topology created through etching. The GF demonstrated a gradual increase from a value of 30.57 in the 0–180% strain range to 54.29 in the 180–350% range. When the strain was extended to 350–450%, the GF sharply escalated to 98.52, corroborating the sensor performance variations under different strain ranges, which is in accordance with the principal explanation provided in Fig. 4b. Of course, we also assessed the capability of the sensor to detect minor deformations. The TPU:PEO/CNTs sensor was capable of responding sensitively to a deformation as low as 1%. As illustrated in Fig. S5 (ESI†), the GF of the TPU:PEO/CNTs sensor within a strain range of 0–10% was 16.39. The sensor also exhibited fast responsiveness, with a reaction time of 220 ms, as depicted in Fig. 5b.

Furthermore, the TPU:PEO/CNTs sensor, designed with an optimized micro–nano structure, not only showed significant performance benefits but also demonstrated notable flexibility and adjustability in its fabrication process. To further assess the universality of this micro–nano topological structure in the conductive material filling process, the TPU/graphene sensor was employed for additional testing. Based on previous experimental results, the TPU/PEO4 composite nanofiber membrane was maintained as the sensor substrate, and the pure-TPU nanofiber membrane served as the control substrate. Using a 3% concentration of graphene dispersion for ultrasonic impregnation, both the TPU/graphene sensor and the TPU:PEO/graphene sensor were tested under identical conditions,

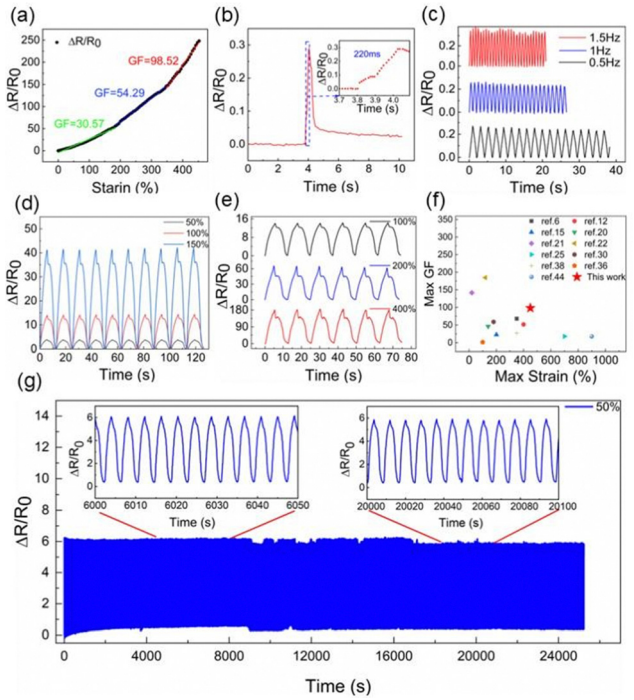

Fig. 5 (a) Diagram of the sensing performance of the TPU:PEO/CNTs strain sensor; (b) response time of the TPU:PEO/CNTs strain sensor; (c) dynamic response of the strain sensor at different stretching rates under 5% strain; (d) $\Delta R/R_0$–time curves of multiple stretching cycles (0–150%) under different strains; (e) relative resistance curves of multiple stretching–release tests performed in different strain ranges (100%, 200% and 400%); (f) comparison of the maximum working range and maximum GF obtained in this work with other references; (g) TPU:PEO/CNTs strain sensor under 6000 cycles at a strain level of 50%.

which displayed promising sensing capabilities as shown in Fig. S6 (ESI†). Nevertheless, the TPU:PEO/graphene sensor with micro–nano topology significantly enhanced its sensing performance, with the resistance change rate increasing nearly tenfold, and the max GF value sharply increased to 976.89 across a 650% strain range. These outcomes further confirm that the porous structure developed in this study effectively improves the adsorption of conductive fillers and is capable of broad application in filler integration.

We systematically investigated the effect of elongation on the performance of TPU:PEO/CNTs strain sensors. The stability of the sensing behavior at different stretching rates was evaluated at a constant strain of 5% at 0.5 Hz, 1 Hz, and 1.5 Hz, respectively. In Fig. 5c, the resistance shows a relatively consistent signal fluctuation at different rates, confirming that the TPU:PEO/CNTs sensor has excellent sensing capabilities under different frequencies of external stimuli. As shown in Fig. 5d, cyclic stretching experiments were conducted at a sensor strain of 50%, 100%, and 150%, all within a GF value of 30.57. Notably, $\Delta R/R_0$ remained consistent at the same strain level but exhibited an increase in response to higher strain levels during multiple cycles, revealing a consistent graphical trend. Subsequently, as depicted in Fig. 5e, the sensor demonstrated reliable performance under numerous strains of 100%, 200%, and 400%, verifying its dynamic response across a broad strain range. Fig. 5f compares the strain range and GF sensitivity of the TPU:PEO/CNTs sensor developed in this study against other recently reported flexible strain sensors. This comparison underscores the remarkable achievements of the TPU:PEO/CNTs sensor in terms of high sensitivity and a wide detection range. For further analysis and comparison, the substrates and conductive materials used in these studies are delineated in Table S1 (ESI†), alongside the maximum GF and strain range noted in each case.

To assess the stability, durability, and repeatability of the sensor, the sensor underwent 6000 stretch–release cycles at 50% strain at a rate of 2 mm min^{-1}. As shown in Fig. 5g, the relative resistance displayed transient behavior due to mechanical hysteresis and changes in the conductive network. However, with the increase in the number of stretching cycles, $\Delta R/R_0$ began to show a downward trend and was gradually stabilized. Therefore, the TPU:PEO/CNTs sensors were demonstrated to possess excellent durability and repeatability, showing their suitability for various applications in the field of flexible strain sensors. Additionally, in testing the stability of the sensor at different temperatures, experiments were conducted at 25 °C and 45 °C. As shown in Fig. S7 (ESI†), the resistance changed slightly at high temperature. Under the same 2.5% stretching, $\Delta R/R_0$ at 45 °C changed slightly, showing an upward trend. As the temperature increased, the CNTs and TPU were more closely combined, thereby improving the sensing performance.

3.5. Application examples of human motion monitoring

The strain sensor developed in this study is composed of TPU:PEO/CNTs and has remarkable properties, including high sensitivity, a wide detection range, and excellent flexibility and stability. The sensor was integrated into a wearable system to assess its practicality and applied on different body areas to monitor signals in real time. As shown in Fig. 6a, the strain sensor was first fixed on the index finger, and obvious signal changes were observed corresponding to different bending amplitudes. In addition, to determine the versatility of the applications, we placed the sensor on the knee joint for gait monitoring. As shown in Fig. 6b, the electrical signal intensity was increased and changed synchronously when the knee joint was bent at different intensities and frequencies, showing the ability of the sensor to distinguish different bending angles.

Furthermore, slight changes can be observed in the sensing curves during knee and wrist bending. This is due to the slight movements of the test subject, highlighting the fast and accurate response of the sensor. It is noteworthy that the sensor can detect subtle movements and capture various aspects of activities, including the movements of surface muscles during drinking, speaking, exhalation, and smiling. As illustrated in Fig. 6c and d, the sensor was attached to the cheek of a subject to monitor facial expressions and to the protruding part of the throat to record subtle changes during drinking or swallowing. The real-time monitoring results show that the sensor can detect human activities and provide detailed information on them, offering a useful method for monitoring behavioral patterns.

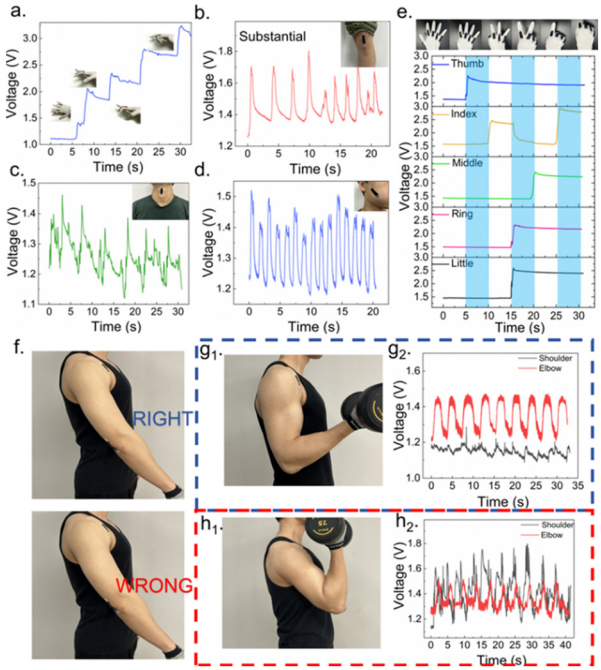

Fig. 6 The use of TPU:PEO/CNTs sensors for monitoring basic human movements such as finger bending (a), knee bending (b), swallowing (c), and smiling (d); (e) five-channel recognition of gestures; (f) bicep curl action sensor pasting position; (g_1) and (g_2) bicep curl correct posture; and (h_1) and (h_2) bicep curl incorrect posture.

To better apply sensors in wearable devices, we designed a multi-channel digital circuit for signal monitoring across multiple sensors. As depicted in Fig. 6e, we attached the sensors to the metacarpophalangeal joints of the five fingers, enabling real-time multi-channel monitoring. The fingers are designed to represent gestures indicating counts from five to zero, respectively. Results showed that the finger signals were sequential, and the changes in electrical signals corresponded accurately with the actual gestures. To further examine the utility of the TPU:PEO/CNTs sensor in human activity monitoring, we conducted tests based on the biceps curl movement, a basic and common fitness exercise suitable for both genders. Here, maintaining correct posture is essential for preventing sports injuries. The sensor system was attached to both shoulder and elbow joints to track muscle movements during the biceps curl exercise, as illustrated in Fig. 6f. When performing biceps curls with correct posture, the biceps muscles are activated, while the shoulders remain stationary, as demonstrated in Fig. $6g_1$. At this juncture, significant sensor activity at the elbow corresponds with the curl motion, while minor changes in the shoulder sensor signal arise chiefly from skin tension, as illustrated in Fig. $6g_2$. However, when the biceps curl posture is incorrect, the elbow moves forward rather than staying fixed. In such cases, the deltoid muscle, responsible for raising and lowering the arm, involuntarily assists, as highlighted in Fig. $6h_1$. Consequently, as depicted in Fig. $6h_2$, the signal during this incorrect posture becomes disorganized. The reliance on the anterior deltoid muscle at the shoulder joint indicates substantial compensatory actions. Such incorrect training postures lessen biceps stimulation and diminish the overall efficacy of the exercise, which may lead to exercise injury. By monitoring these deviations through the TPU:PEO/CNTs sensor responses, corrections in movement postures can be guided, underscoring the significant potential of the sensor as a sports assistant in wearable devices.

To examine the stability of the sensor under sweating, we employed a 1% sodium chloride solution to mimic sweat and documented the changes in sensor resistance that followed drying, sweat infiltration, and evaporation. This process was repeated three times, applying approximately 0.5 mL of the simulated sweat sprinkling onto the sensor using a spray bottle. As indicated in Fig. S8 (ESI†), the resistance of the sensor rapidly increased upon being sprinkled with sweat but returned to nearly its original level after the sweat evaporated. After three cycles of simulated sweat exposure and evaporation, the stability of the sensor under sweaty conditions was substantiated further. Additionally, the sensing performance of the sensor was tested under conditions of 80% strain following each cycle of sweat evaporation. According to Fig. S9 (ESI†), each cycle of sweat exposure and drying influenced the waveform of the sensor but still maintained consistent sensitivity. Thus, although sweat exposure momentarily slightly affected the resistance of the sensor, it restored swiftly following sweat evaporation, exerting minimal impact on sensor sensitivity.

4. Conclusions

In summary, we developed a TPU:PEO/CNTs sensor featuring a micro–nano topology created through an etching process, achieving a GF of 98.52 within 450% strain. This sensor maintains robust stability and durability after enduring 6000 cycles. Furthermore, a wider detection range (0–650%) and higher sensitivity (GFmax = 976.89) are obtained for the TPU:-PEO/graphene sensor, demonstrating the effectiveness of the etching method for versatile strain sensors. It accurately tracks human movement and vital signs, effectively operates across varying temperatures, and simulates sweat conditions. Moreover, it can discern multi-channel signals, making it well-suited for integration into wearable devices for monitoring gestures and fitness postures. Results indicate that the highly tensile and sensitive strain sensors are promising for practical applications in wearable devices that provide the possibility to monitor human activity in real-time.

Author contributions

All authors discussed and contributed to the interpretation of the results and the final manuscript. W. X. L. and Q. Q. D. designed the experiments and wrote the manuscript. T. Z. assisted in the FTIR measurements. Z. L. G. and W. B. S. assisted in the multi-channel digital circuit design. Y. J. L. and Y. Y. L. supervised this project. Z. H. W. and B. W. participated in the manuscript revision. All authors have approved the final version of the manuscript.

Data availability

The data supporting this article have been included as part of the ESI.†

Conflicts of interest

There are no conflicts to declare.

Acknowledgements

This work was financially supported by the Natural Science Foundation of He'nan Province - Excellent Youth Scholar (232300421092) and the National Natural Science Foundation of China (62005152 and 61973206).

Notes and references

1 Y. Shen, W. Yang, F. Hu, X. Zheng, Y. Zheng, H. Liu, H. Algadi and K. Chen, *Adv. Compos. Hybrid Mater.*, 2023, **6**, 21.
2 H. Dong, J. Sun, X. Liu, X. Jiang and S. Lu, *ACS Appl. Mater. Interfaces*, 2022, **14**, 15504–15516.
3 J. V. Vaghasiya, C. C. Mayorga-Martinez and M. Pumera, *npj Flexible Electron.*, 2023, **7**, 26.
4 W. Sun, Z. Guo, Z. Yang, Y. Wu, W. Lan, Y. Liao, X. Wu and Y. Liu, *Sensors*, 2022, **22**, 7784.
5 M. Cui, S. Wu, J. Li, Y. Zhao, W. Zhai, K. Dai, C. Liu and C. Shen, *Compos. Sci. Technol.*, 2023, **244**, 110309.
6 P. Zhang, W. Li, Q. Zhang, X. Wang, G. Lin, W. Li, Y. Li, K. Zhang and L. Huang, *IEEE Sens. J.*, 2023, **23**, 1497–1506.
7 F. Han, T. Wang, G. Liu, H. Liu, X. Xie, Z. Wei, J. Li, C. Jiang, Y. He and F. Xu, *Adv. Mater.*, 2022, **34**, 2109055.
8 Y. Yu, Y. Feng, F. Liu, H. Wang, H. Yu, K. Dai, G. Zheng and W. Feng, *Small*, 2023, **19**, 2204365.
9 T. Q. Trung and N. Lee, *Adv. Mater.*, 2016, **28**, 4338–4372.
10 L. Liu, S. Niu, J. Zhang, Z. Mu, J. Li, B. Li, X. Meng, C. Zhang, Y. Wang, T. Hou, Z. Han, S. Yang and L. Ren, *Adv. Mater.*, 2022, **34**, 2200823.
11 R. Rahimi, M. Ochoa, W. Yu and B. Ziaie, *ACS Appl. Mater. Interfaces*, 2015, **7**, 4463–4470.
12 H. Nie, Z. Chen, H. Tang, Y. Ren and W. Liu, *Polym. Compos.*, 2024, **45**, 5522–5531.
13 Y. Bai, L. Yin, C. Hou, Y. Zhou, F. Zhang, Z. Xu, K. Li and Y. Huang, *Adv. Funct. Mater.*, 2023, **33**, 2214119.
14 X. Yue, C. Fang, Q. Yao, C. Liu, C. Shen and H. Liu, *Chem. Eng. J.*, 2024, **491**, 151853.
15 S. Peng, S. Wu, Y. Yu, P. Blanloeuil and C. H. Wang, *J. Mater. Chem. A*, 2020, **8**, 20531–20542.
16 S. Naderizadeh, G. Santagiuliana, W. Tu, D. Marsh, E. Bilotti and J. J. C. Busfield, *IEEE Sens. J.*, 2023, **23**, 18013–18021.
17 L. Wang, J. Wang, C. Fan, T. Xu and X. Zhang, *Chem. Eng. J.*, 2023, **455**, 140609.
18 H. Sun, Y. Bu, H. Liu, J. Wang, W. Yang, Q. Li, Z. Guo, C. Liu and C. Shen, *Sci. Bull.*, 2022, **67**, 1669–1678.
19 L. Zhang, M. Wu, Q. Liu and H. Wang, *Nanotechnol. Rev.*, 2023, **12**, 20230119.
20 L. Xing, L. Li, Y. Liu, J. Ren, G. Guo, Y. Chen, Y. Zheng and B. Sun, *J. Mater. Chem. A*, 2024, **12**, 10905–10912.
21 X. Chen, Z. Yin, Y. Deng, Z. Li, M. Xue, Y. Chen, Y. Xie, W. Liu, P. He, Y. Luo, Z. Hong and C. Xie, *Sens. Actuators, A*, 2023, **362**, 114630.
22 F. Liu, D. Xie, F. Lv, L. Shen, Z. Tian and J. Zhao, *ACS Appl. Nano Mater.*, 2023, **6**, 4522–4531.
23 Y. Bai, C. Hou, W. Cheng, Z. Xu, K. Li and Y. Huang, *Program. Mater.*, 2024, **2**, e3.
24 E. H. Backes, S. V. Harb, L. A. Pinto, N. K. De Moura, G. F. De Melo Morgado, J. Marini, F. R. Passador and L. A. Pessan, *J. Mater. Sci.*, 2024, **59**, 1123–1152.
25 Y. Tian, M. Huang, Y. Wang, Y. Zheng, R. Yin, H. Liu, C. Liu and C. Shen, *Chem. Eng. J.*, 2024, **480**, 147899.
26 L. Liu, T. Luo, X. Kuang, X. Wan, X. Liang, G. Jiang, H. Cong and H. He, *ACS Sens.*, 2024, **9**, 2476–2487.
27 Z. Jia, Z. Li, S. Ma, W. Zhang, Y. Chen, Y. Luo, D. Jia, B. Zhong, J. M. Razal, X. Wang and L. Kong, *J. Colloid Interface Sci.*, 2021, **584**, 1–10.
28 Y. Bu, T. Shen, W. Yang, S. Yang, Y. Zhao, H. Liu, Y. Zheng, C. Liu and C. Shen, *Sci. Bull.*, 2021, **66**, 1849–1857.
29 Q. Gao, Z. Chen, C. Liu, Y. Wang, J. Zhu and C. Gao, *J. Alloys Compd.*, 2024, **980**, 173547.
30 W. Luo, W. Fei, L. Yang, Y. Chen and Y. Wen, *J. Coat. Technol. Res.*, 2020, **17**, 1157–1169.
31 J. Ai, Q. Wang, Z. Li, D. Lu, S. Liao, Y. Qiu, X. Xia and Q. Wei, *ACS Appl. Mater. Interfaces*, 2024, **16**, 1428–1438.
32 S. Chen, J. Li, H. Liu, W. Shi, Z. Peng and L. Liu, *Chem. Eng. J.*, 2022, **430**, 133005.
33 P. Qiu, R. Jin, Y. Son, A. Ju, W. Jiang, L. Wang and W. Luo, *Adv. Fiber Mater.*, 2024, **6**, 658–685.
34 X. Han, T. Lu, H. Wang, Z. Zhang and S. Lu, *ACS Sustainable Chem. Eng.*, 2023, **11**, 13756–13764.
35 Y. Xin, Y. Lou, X. Mao, X. Jia, R. Li, P. Yu and X. Ban, *Macromol. Rapid Commun.*, 2023, **44**, 2300307.
36 E. Zhuo, Z. Wang, X. Chen, J. Zou, Y. Fang, J. Zhuo, Y. Li, J. Zhang and Z. Gong, *Polymers*, 2023, **15**, 2934.
37 P. Mohamadi, E. Mohsenzadeh, C. Cochrane and V. Koncar, *IEEE Sens. J.*, 2023, **23**, 24308–24315.
38 X. Cui, H. Xie, Y. Jiang, Z. Xu, G. Sui and X. Yang, *Polym. Adv. Technol.*, 2023, **34**, 3011–3021.
39 J. Ai, S. Cheng, Y. Miao, P. Li and H. X. Zhang, *Carbon*, 2023, **205**, 454–462.
40 Q. Yuan, H. Jiang, T. Gao, S. Zhang, S. Jia, T. Wu and J. Qu, *J. Mater. Chem. A*, 2023, **11**, 7447–7456.
41 B. Niu, S. Yang, Y. Yang and T. Hua, *SmartMat*, 2023, **4**, e1178.
42 J. Wang, H. Liu, X. Yue, D. Zhang, R. Yin, H. Sun, C. Liu and C. Shen, *Mater. Today Nano*, 2023, **24**, 100427.
43 H. Liu, M. Dong, W. Huang, J. Gao, K. Dai, J. Guo, G. Z. C. Liu, C. Shen and Z. Guo, *J. Mater. Chem. C*, 2017, **5**, 73.
44 M. Ren, Y. Zhou, Y. Wang, G. Zheng, K. Dai, C. Liu and C. Shen, *J. Chem. Eng.*, 2019, **360**, 762–777.